



# Unveiling the high activity origin of NiFe catalysts decorated Ta<sub>3</sub>N<sub>5</sub> photoanodes for oxygen evolution reaction

Congzhao Dong<sup>a,b,1</sup>, Xian Zhang<sup>b,1</sup>, Yong Ding<sup>a,\*</sup>, Yajun Zhang<sup>b</sup>, Yingpu Bi<sup>b,\*</sup>

<sup>a</sup> State Key Laboratory of Applied Organic Chemistry, Key Laboratory of Advanced Catalysis of Gansu Province, College of Chemistry and Chemical Engineering, Lanzhou University, Lanzhou 730000, PR China

<sup>b</sup> State Key Laboratory for Oxo Synthesis & Selective Oxidation, Lanzhou Institute of Chemical Physics, CAS, Lanzhou 730000, PR China

## ARTICLE INFO

### Keywords:

Solar Energy  
Water Splitting  
Photoanode  
Oxygen Evolution  
Catalyst

## ABSTRACT

Bimetallic NiFe catalysts could effectively promote the photoelectrochemical (PEC) water splitting activities of Ta<sub>3</sub>N<sub>5</sub> photoanodes, while exploring the intrinsic activity origin is crucial for constructing highly efficient solar-energy conversion systems. Herein, we demonstrate a simple impregnation strategy for rational deposition of NiFe catalysts nanolayers on Ta<sub>3</sub>N<sub>5</sub> nanotube photoanodes, which achieved a superior photocurrent density of 11.2 mA cm<sup>-2</sup> at 1.23 V versus the reversible hydrogen electrode (RHE) accompanied by a low onset potential (0.3 V<sub>RHE</sub>). More importantly, systematic studies reveal that the preferred deposition of Fe catalysts nanolayers on Ta<sub>3</sub>N<sub>5</sub> photoanode surfaces could effectively promote the charge separation and hole transfer, while the subsequent formation of Ni catalysts nanolayers could provide the catalytic active-sites for water oxidation. Accordingly, their synergistic effects significantly improve the interfacial hole transfer and surface oxygen evolution kinetics, leading to an outstanding PEC water splitting activity. This work not only clarifies the intrinsic high-activity origins of NiFe/Ta<sub>3</sub>N<sub>5</sub> photoanodes, but also provides new insights into the rational construction of highly efficient OER catalysts for PEC water splitting.

## 1. Introduction

Photoelectrochemical (PEC) water splitting has been regarded as a promising approach to convert the intermittent solar energy into renewable and clean hydrogen fuels [1–4]. Constructing PEC system with high conversion efficiencies is highly desirable for solar fuel production [5–8]. However, the PEC conversion efficiencies have been severely restricted by the oxygen evolution half-reaction occurred on semiconductor photoanodes [9–11]. Thereby, the rational design and fabrication of highly efficient photoanodes for OER are crucial for achieving the future practical applications [12–14]. Among various semiconductors, tantalum nitride (Ta<sub>3</sub>N<sub>5</sub>) has been extensively recognized as an attractive photoanode material, owing to its ideal bandgap (2.0–2.1 eV) suitable for the solar-light absorption and high theoretical maximum solar conversion efficiency (15.9%) [15,16]. However, the PEC water splitting performances of reported Ta<sub>3</sub>N<sub>5</sub>-based photoanodes were generally far below the theoretical expectation, mainly suffered from the high charge recombination, excess surface states, and poor surface reactivity [17–19]. Recently, various strategies, including

element-doping [20–24], hetero-construction [25–27], and morphology-tailoring [28,29], have been extensively reported to enhance the PEC water oxidation activity of Ta<sub>3</sub>N<sub>5</sub> photoanodes, and some important progresses have been made during the past decade. However, the intrinsically surface charge recombination and poor surface active-sites still inhered in these Ta<sub>3</sub>N<sub>5</sub> photoanodes, leading to the high onset potential and poor PEC conversion efficiencies.

Recently, the decoration of OER catalysts has been extensively reported for significantly improving the PEC performances of Ta<sub>3</sub>N<sub>5</sub> photoanodes [30,31]. More specifically, these OER catalysts could effectively reduce the charge recombination at the photoanode/electrolyte interface and provide favorable active sites for OER to minimize overpotential [32]. Among various candidates, metal oxides or oxyhydroxides, especially for Ni [33–35], Fe [36–38], and Co [39–43], have been widely reported as efficient OER catalysts to promote the PEC activities. For example, Pihosh et al. reported the Ta<sub>3</sub>N<sub>5</sub> nanorods photoanodes homogeneously covered by the NiFeO<sub>x</sub> catalyst, which exhibited a saturated photocurrent density of 9.95 mA cm<sup>-2</sup> at 1.05 V<sub>RHE</sub> [44]. Shi et al. employed an electrodeposition method for

\* Corresponding authors.

E-mail addresses: [dingyong1@lzu.edu.cn](mailto:dingyong1@lzu.edu.cn) (Y. Ding), [yingpubi@licp.cas.cn](mailto:yingpubi@licp.cas.cn) (Y. Bi).

<sup>1</sup> These authors contributed equally to this work

loading  $\text{Ni}_{0.9}\text{Fe}_{0.1}\text{OOH}$  catalyst on  $\text{Ta}_3\text{N}_5$  photoanodes, and a photocurrent density of  $5.6 \text{ mA cm}^{-2}$  at  $1.23 \text{ V}_{\text{RHE}}$  has been achieved [45]. Especially, Liu et al. reported a porous cubic  $\text{Ta}_3\text{N}_5$  film incorporated with a  $\text{TiO}_x$  layer, a ferrihydrite layer, a  $\text{Ni}(\text{OH})_x$  layer, Co complex and Ir complex, which exhibits an approach-limit photocurrent density of  $12.1 \text{ mA cm}^{-2}$  [46]. Despite tremendous efforts on the development of bimetallic OER catalysts, their fundamental roles, especially for NiFe catalysts, in determining the PEC water splitting activities still remain ambiguous until now. Thereby, an in-depth fundamental understanding is essential for rational design and construction of highly efficient  $\text{Ta}_3\text{N}_5$ -based PEC water splitting system.

In this work, we demonstrated a simple impregnation method to uniformly decorate NiFe catalysts on  $\text{Ta}_3\text{N}_5$  nanotube photoanodes, and an outstanding PEC performance for water oxidation ( $11.2 \text{ mA cm}^{-2}$ ,  $1.23 \text{ V}_{\text{RHE}}$ ) has been achieved under the simulated sunlight irradiation (AM 1.5 G,  $100 \text{ mW cm}^{-2}$ ). Detailed analysis reveals that the preferentially deposited Fe catalysts layers could efficiently extract holes from  $\text{Ta}_3\text{N}_5$  photoanodes, while subsequently deposited Ni catalysts layers exhibited stronger catalytic ability for water oxidation. Owing to their synergistic effects, the PEC performances of  $\text{Ta}_3\text{N}_5$  nanotube for water oxidation have been significantly improved. These demonstrations offer a new insight into the crucial roles of bimetallic OER catalysts on  $\text{Ta}_3\text{N}_5$  photoanodes, which may have significant implications for the design and construction of highly efficient PEC water splitting devices.

## 2. Experiment section

### 2.1. Materials and chemical reagents

Ta foil (99.99%) was obtained from Hebei Chengshuo. Sulfuric acid ( $\text{H}_2\text{SO}_4$ ), ammonium fluoride ( $\text{NH}_4\text{F}$ , >96%), iron chloride hexahydrate ( $\text{FeCl}_3 \cdot 6 \text{ H}_2\text{O}$ , 99%), nickel chloride hexahydrate ( $\text{NiCl}_2 \cdot 6 \text{ H}_2\text{O}$ , 99%), tannic acid, sodium hydroxide ( $\text{NaOH}$ , 99%), and potassium hydroxide ( $\text{KOH}$ , >85%) were obtained from Sinopharm Chemical Reagent Co., Ltd. Deionized water with a resistivity of  $18.25 \text{ M}\Omega\text{-cm}$  was used in all reactions.

### 2.2. Instruments

Scanning electron microscopy measurements were performed on a field-emission scanning electron microscope (SEM, JSM-6701 F, JEOL) operated at an accelerating voltage of 5 kV. Transmission electron microscopy (TEM) measurements were determined by using a FEI Tecnai TF20 microscope operated at 200 kV. The crystalline structures were identified by X-ray diffraction analysis (XRD, Smartlab-SE) using  $\text{Cu K}\alpha$  radiation at 50 kV and 50 mA. The elemental composition and chemical valence states were identified by X-ray photoelectron spectroscopy (XPS, ESCALAB 250Xi). Scanning photoelectrochemical microscopy (SPECM, AMETEK, USA) measurements were carried out on a simulated sunlight (AM 1.5 G)/SECM platform. The height distribution images and surface potential images of the samples were measured using Kelvin probe force microscopy (KPFM, Bruker) under an ambient atmosphere. The zeta potential was measured using Malvern Zetasizer ZEN 3600 at 293 K.

### 2.3. Preparation of $\text{Ta}_3\text{N}_5$

$\text{Ta}_3\text{N}_5$  was prepared by a Chemical Vapor Deposition (CVD) method as our group previous reported [47]. Typically, four piece of cleaned Ta foils ( $0.2 \text{ mm} \times 10 \text{ mm} \times 25 \text{ mm}$ ) were put into the muffle furnace at  $590^\circ\text{C}$  for 30 min [48]. The heating rate was set as  $5^\circ\text{C min}^{-1}$ . After the heating process, the planar  $\text{Ta}_2\text{O}_5$  nanofilms were cooled down to room temperature. Vertical aligned  $\text{Ta}_2\text{O}_5$  nanotubes were prepared by anodizing Ta foil ( $0.2 \text{ mm} \times 10 \text{ mm} \times 50 \text{ mm}$ ) in a two-electrochemical cell [49]. Prior to anodization, Ta foils were polished with  $\text{Al}_2\text{O}_3$  paper and then ultrasonicated in deionized water (10 min), ethanol (10

min) and acetone (10 min) for cleaning. After dried in air, one side of Ta foil was coated by scotch tape. Samples and Pt wire were used as work electrode and counter electrode, respectively, in a sulfuric acid electrolyte consisting of 172.8 mL sulfuric acid, 2.76 g  $\text{NH}_4\text{F}$  and 27.2 mL deionized water for anodization. The anodization process was performed at a constant voltage of 60 V at room temperature using a programmable DC power supply (Interlock IPD-12003SLU). The first  $\text{Ta}_2\text{O}_5$  nanotubes were mechanical exfoliated by scotch tape, and washed by deionized water and dried subsequently. The underlying Ta was explored and then subjected to a second anodization process at 60 V for 3 min. The  $\text{Ta}_2\text{O}_5$  nanotubes were washed by deionized water and dried subsequently, and then cut into size of  $0.2 \text{ mm} \times 10 \text{ mm} \times 25 \text{ mm}$ .

Then, four piece of planar  $\text{Ta}_2\text{O}_5$  nanofilms were put into a porcelain boat in the left side of CVD system (a single temperature zone tube furnace, HF-Kejing, OTF-1200X),  $\text{Ta}_2\text{O}_5$  nanotubes were put into another porcelain boat in the right side. The distance between the two porcelain is fixed at 6 cm.  $\text{NH}_3$  was ventilated from left to right. The system was charged with  $\text{NH}_3$  for 5 min before heating and the  $\text{NH}_3$  flow rate was 800 sccm.  $\text{Ta}_2\text{O}_5$  were annealed at  $1000^\circ\text{C}$  with a heating rate of  $10^\circ\text{C min}^{-1}$  under  $\text{NH}_3$  flow (400 sccm) and kept for 1 h, and then cooled naturally and finally  $\text{Ta}_3\text{N}_5$  was obtained.

### 2.4. Decoration with NiFe-based catalysts on $\text{Ta}_3\text{N}_5$

NiFe-based catalysts was prepared by a simple impregnation method with some modifications [50]. The as-prepared  $\text{Ta}_3\text{N}_5$  photoanodes were immersed in 10 mL mixed aqueous solution (7.5 mL 10 mM  $\text{NiCl}_2$  and 2.5 mL 10 mM  $\text{FeCl}_3$ ) for 15 min. Then, 10 mL tannin aqueous solution ( $9 \text{ g}\cdot\text{L}^{-1}$ ) and 50  $\mu\text{L}$   $\text{NaOH}$  aqueous solution (2 M) were subsequently added into the mixed solution under stirring at 180 rpm for 5 min. The mixed solution was left to stand for 1 h at 303 K. Finally, the samples were washed with deionized water and dried in air. The integrate photoanode was noted as NiFe/ $\text{Ta}_3\text{N}_5$ .

Similarly, the  $\text{Ta}_3\text{N}_5$  photoanodes were immersed in 10 mL  $\text{NiCl}_2$  or  $\text{FeCl}_3$  and other conditions were the same, the sample obtained was noted as Ni/ $\text{Ta}_3\text{N}_5$  or Fe/ $\text{Ta}_3\text{N}_5$ . For experiments with different deposition sequences of Ni and Fe, when the  $\text{Ta}_3\text{N}_5$  was first immersed in 10 mL  $\text{FeCl}_3$  while other conditions remain unchanged, and then the obtained Fe/ $\text{Ta}_3\text{N}_5$  was immersed in 10 mL  $\text{NiCl}_2$  with the same other conditions, the final sample was noted as Ni/Fe/ $\text{Ta}_3\text{N}_5$ . Conversely, when the deposition sequence was Ni catalyst first and then Fe catalyst, the obtained sample was noted as Fe/Ni/ $\text{Ta}_3\text{N}_5$ .

### 2.5. Photoelectrochemical measurements

PEC measurements of photoanodes were performed in a typical three-electrode configuration using an electrochemical workstation (CHI760E) under simulated AM 1.5 G ( $100 \text{ mW cm}^{-2}$ ) illumination provided by a solar simulator (300 W Xe with optical filter). The fabricated photoanode, a Pt sheet ( $1 \text{ cm} \times 1 \text{ cm}$ ) and an Ag/AgCl (3 M KCl) were used as working electrode, counter electrode and reference electrode, respectively. The measured potentials were converted to the reversible hydrogen electrode (RHE) using the equation below.

$$E_{\text{RHE}} = E_{\text{Ag/AgCl}} + 0.059 \text{ pH} + E_{\text{Ag/AgCl}}^0$$

Where  $E_{\text{Ag/AgCl}}^0$  is  $0.197 \text{ V}$  at  $25^\circ\text{C}$ . PEC experiments were carried out in a 1 M  $\text{KOH}$  aqueous solution ( $\text{pH} = 13.6$ ). The photocurrent was performed by linear sweep voltammetry (LSV) by scanning potential from  $-0.8$ – $0.3 \text{ V}$  (vs. Ag/AgCl) with a scan rate of  $10 \text{ mV/s}$ . The illuminated areas were  $0.385 \text{ cm}^2$  with a mask.

The applied bias photon-to-current efficiency (ABPE) was calculated by following equation:

$$\text{ABPE}(\%) = \frac{I \times (1.23 - V_{\text{bias}})}{P_{\text{light}}}$$

where  $I$  is the photocurrent density,  $V_{bias}$  is the applied potential,  $P_{light}$  is the incident illumination power density ( $100 \text{ mW cm}^{-2}$ ).

The current responsiveness of  $\text{Ta}_3\text{N}_5$  photoanodes to light of different wavelengths test was conducted using a xenon lamp (Oriel 6365, 150 W) and a motorized monochromator (Oriel Cornerstone7400). The test was measured at 0 V vs. Ag/AgCl with 10 nm steps in the wavelength range 300–700 nm.

The photocurrent densities ( $J_c$ ) were calculated by integrating the incident photon-to-current efficiency (IPCE) values with the standard solar spectrum (ASTMG-173–03) using the following equation:

$$J_c = \int_{300}^{650} \frac{\lambda \times IPCE(\lambda) \times E(\lambda)}{1240} d(\lambda)$$

Specifically,  $\lambda$  and  $E(\lambda)$  represent the light wavelength (nm) and the corresponding power density ( $\text{mW cm}^{-2}$ ), respectively.

Electrochemical impedance spectroscopy (EIS) was monitored at a frequency range of  $10^5$  to 0.1 Hz with an amplitude of 5 mV at 0.8  $V_{RHE}$  under AM 1.5 G illumination.

### 3. Results and discussion

#### 3.1. Morphology and structure characterization

Tantalum nitride ( $\text{Ta}_3\text{N}_5$ ) nanotube arrays supported on metallic tantalum (Ta) substrates were fabricated by the combination of anodic oxidation and ammonia treatment. Their morphology and structure were explored by scanning electron microscopy (SEM). The typical SEM images shown in Fig. S1A clearly reveal their uniform tubular nanostructure with an average wall thickness of about 30 nm and a main pore diameter of 100 nm. Furthermore, the cross-sectional SEM images (Fig. S1B) demonstrate that the  $\text{Ta}_3\text{N}_5$  nanotube arrays have been vertically grown on the conductive substrate. Subsequently, a facile solution immersion method was employed to decorate NiFe

oxyhydroxides on  $\text{Ta}_3\text{N}_5$  nanotube photoanodes (marked as NiFe/ $\text{Ta}_3\text{N}_5$ ). Fig. 1A shows the typical top-view and cross-section SEM images of NiFe/ $\text{Ta}_3\text{N}_5$  photoanodes, respectively, clearly indicating that no evident morphology or structure change could be observed compared with the pristine  $\text{Ta}_3\text{N}_5$  photoanodes.

Transmission electron microscopy (TEM) has also been performed to explore their surface morphology and structure. As shown in Fig. 1B, the obtained NiFe/ $\text{Ta}_3\text{N}_5$  samples exhibit a hollow and porous tubular nanostructure. Furthermore, the high-resolution TEM image (Fig. 1C) clearly demonstrates the lattice spacing of 0.342 and 0.249 nm, respectively, which could be well indexed to (111) and (113) crystal planes of  $\text{Ta}_3\text{N}_5$  (JCPDS No. 89–5200). Note that compared with pristine  $\text{Ta}_3\text{N}_5$  explore their surface morphology and structure. As shown in Fig. 1B, the obtained NiFe/ $\text{Ta}_3\text{N}_5$  samples exhibit a hollow and porous tubular nanostructure. Furthermore, the high-resolution TEM image (Fig. 1C) clearly demonstrates the lattice spacing of 0.342 and 0.249 nm, respectively, which could be well indexed to (111) and (113) crystal planes of  $\text{Ta}_3\text{N}_5$  (JCPDS No. 89–5200). Note that compared with pristine  $\text{Ta}_3\text{N}_5$  (Fig. S1D), a uniform amorphous nanolayer with a thickness of  $\sim 3$  nm has been uniformly deposited on  $\text{Ta}_3\text{N}_5$  nanotube surfaces, which should be attributed to the formation of NiFe catalysts.

Energy dispersive X-ray spectroscopy (EDS) elemental mapping has been conducted to further explore their chemical composition and structure. As shown in Fig. 1D, the evident signals of Ta, N, O, Ni and Fe elements could be detected in the whole regions, confirming the uniform distribution of NiFe catalysts on  $\text{Ta}_3\text{N}_5$  nanotubes. Furthermore, the Ni and Fe elements have been explored by inductively coupled plasma-optic emission spectroscopy (ICP-OES), and an atom ratio of 1:3.3 for Ni and Fe has been obtained. The X-ray diffraction (XRD) patterns (Fig. S5) show that the main peaks could be ascribed to  $\text{Ta}_3\text{N}_5$  crystal phase (JCPDS No. 89–5200), while some diffraction peaks of  $\text{Ta}_2\text{N}$  phase (JCPDS No. 26–0985) and  $\text{Ta}_{0.1}\text{N}$  phase (JCPDS No. 25–1278) could also be detected. This phenomenon should be attributed to the formation of a transitional layer between the  $\text{Ta}_3\text{N}_5$  and Ta substrate during the

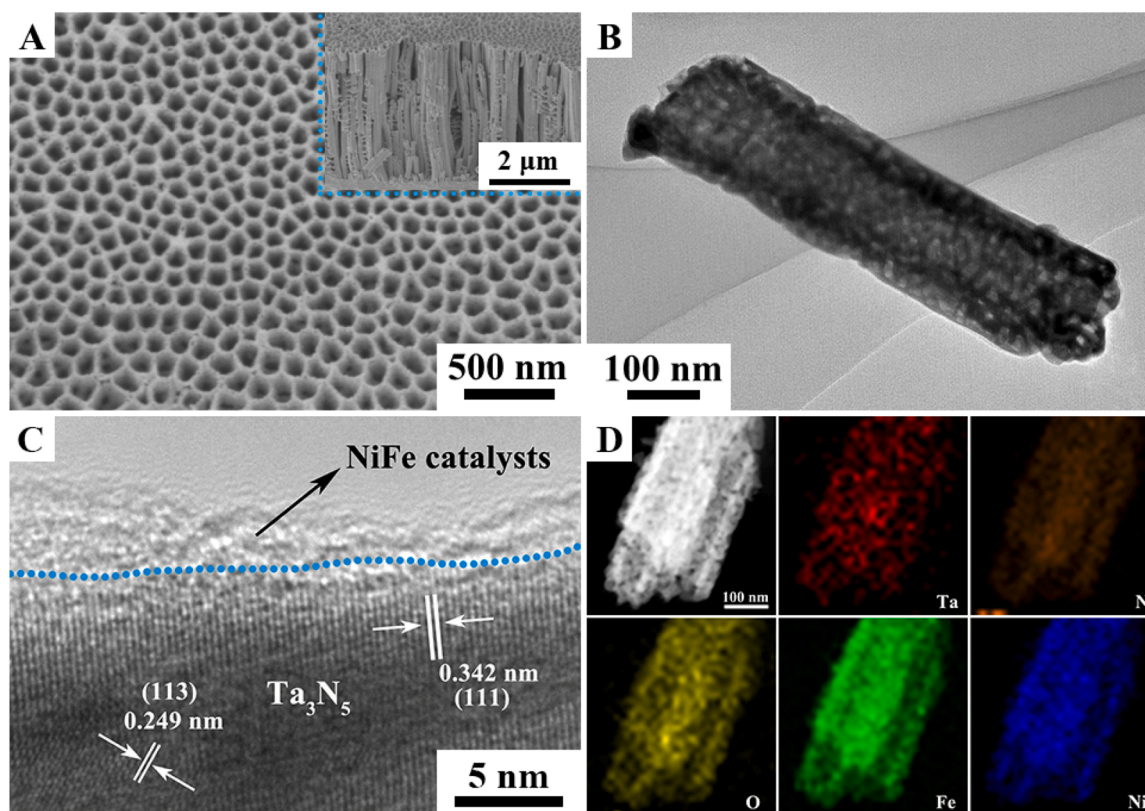


Fig. 1. (A) Top-view SEM image, (B) TEM, (C) HRTEM and (D) elemental mapping image of the NiFe/ $\text{Ta}_3\text{N}_5$  photoanode. The inset in A is cross-view SEM image.



ammonia treatment. However, note that no evident diffraction peaks of NiFe catalysts could be detected in the obtained NiFe/Ta<sub>3</sub>N<sub>5</sub> photoanodes, possibly owing to their amorphous structure, ultrathin thickness, and uniform distribution.

### 3.2. Photoelectrochemical activity and mechanism analysis

PEC water splitting performances of above samples were explored in 1 M KOH electrolyte (pH=13.6) under AM 1.5 G simulated sunlight (100 mW cm<sup>-2</sup>). For comparison, the pristine Ta<sub>3</sub>N<sub>5</sub>, Ni/Ta<sub>3</sub>N<sub>5</sub>, Fe/Ta<sub>3</sub>N<sub>5</sub> photoanodes have also been fabricated and measured under same conditions. The linear-sweep voltammogram (LSV) curves shown in Fig. 2A clearly reveal that the pristine Ta<sub>3</sub>N<sub>5</sub> photoanodes exhibit a

relatively low photocurrent density (1.3 mA cm<sup>-2</sup> at 1.23 V<sub>RHE</sub>), mainly suffering from the high charge recombination and sluggish oxygen evolution kinetics. Obviously, the decoration of Ni or Fe catalysts on Ta<sub>3</sub>N<sub>5</sub> photoanodes could effectively promote the PEC water oxidation activity, and the photocurrent densities have been increased up to 3.5 mA cm<sup>-2</sup> and 2.9 mA cm<sup>-2</sup> at 1.23 V<sub>RHE</sub>, respectively. Amazingly, an outstanding photocurrent density of 11.2 mA cm<sup>-2</sup> at 1.23 V<sub>RHE</sub> has been achieved over NiFe/Ta<sub>3</sub>N<sub>5</sub> photoanodes accompanied by a lower onset potential (measured at 20 μA cm<sup>-2</sup>) for OER (0.3 V<sub>RHE</sub>). These demonstrations clearly reveal that the synergistic effects of NiFe catalysts could significantly promote the oxygen evolution activity of Ta<sub>3</sub>N<sub>5</sub> photoanodes. In addition, their applied bias photon to current efficiencies (ABPE) have been calculated from the above LSV curves and

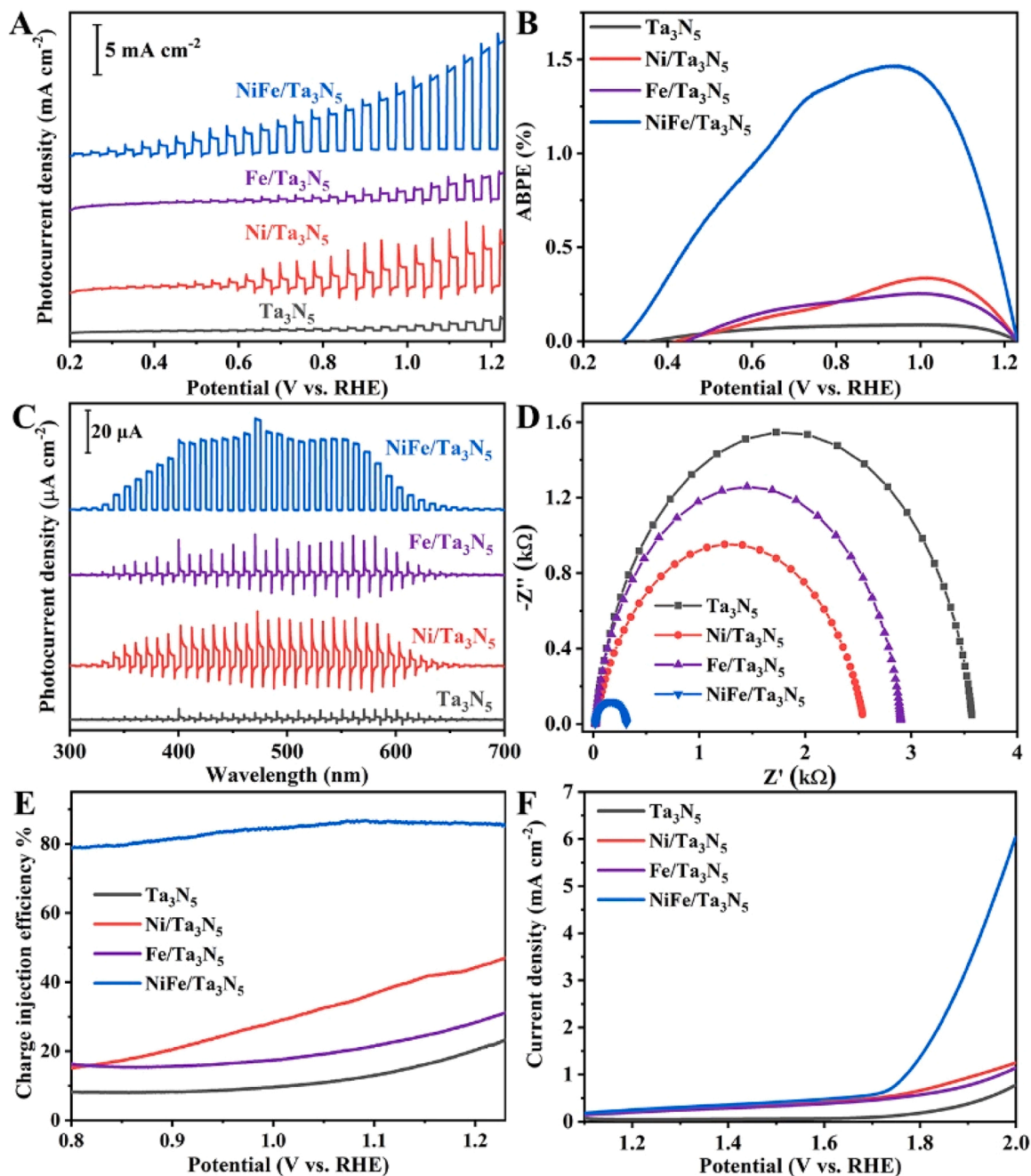


**Fig. 2.** (A) Linear-sweep voltammogram (LSV) curves, (B) the applied bias photon-to-current efficiency (ABPE), (C) current density under illumination with different wavelength at 1.0 V<sub>RHE</sub>, (D) electrochemical impedance spectroscopy (EIS) at 0.8 V<sub>RHE</sub> under illumination, (E) charge injection efficiency and (F) oxygen evolution reaction in dark for Ta<sub>3</sub>N<sub>5</sub>, Ni/Ta<sub>3</sub>N<sub>5</sub>, Fe/Ta<sub>3</sub>N<sub>5</sub> and NiFe/Ta<sub>3</sub>N<sub>5</sub> photoanodes. All the tests were conducted in 1 M KOH (pH 13.6) electrolyte.



shown in Fig. 2B. Obviously, NiFe/Ta<sub>3</sub>N<sub>5</sub> photoanodes exhibit a maximum ABPE value of 1.46% at 0.94 V<sub>RHE</sub>, which is much higher than that of pristine Ta<sub>3</sub>N<sub>5</sub> (0.09% at 1.02 V<sub>RHE</sub>), Ni/Ta<sub>3</sub>N<sub>5</sub> (0.34% at 1.02 V<sub>RHE</sub>), and Fe/Ta<sub>3</sub>N<sub>5</sub> (0.25% at 1.01 V<sub>RHE</sub>), respectively.

Photocurrent responses of all-prepared Ta<sub>3</sub>N<sub>5</sub> photoanodes at different wavelengths were performed and shown in Fig. 2C. Owing to the high charge recombination and sluggish OER kinetics, the pristine Ta<sub>3</sub>N<sub>5</sub> photoanodes demonstrate the relatively poor photocurrent response in the whole wavelength ranges. After the decoration of Ni or Fe catalysts, the photocurrent response of Ta<sub>3</sub>N<sub>5</sub> photoanodes could be effectively promoted. More specifically, the high photo-response of Fe/Ta<sub>3</sub>N<sub>5</sub> photoanodes could not be efficiently maintained and rapidly decreased. This phenomenon clearly indicates that Fe catalysts could effectively promote the charge separation and hole transfer, while possess relatively poor catalytic activity for water oxidation, resulting in the recombination of the separated electron and hole once again. Compared with Fe/Ta<sub>3</sub>N<sub>5</sub> photoanodes, Ni/Ta<sub>3</sub>N<sub>5</sub> photoanodes exhibit a more stable photocurrent response, indicating their relatively higher catalytic activity for water oxidation. Interestingly, both high and stable photocurrent response could be achieved on NiFe/Ta<sub>3</sub>N<sub>5</sub> photoanodes in the whole wavelength ranges, indicating that the NiFe catalysts not only promote the charge separation, but also provide the catalytic active sites for oxygen evolution. As shown in Fig. S6, the calculated photocurrent density for NiFe/Ta<sub>3</sub>N<sub>5</sub> photoanodes is 6.05 mA cm<sup>-2</sup> at 1.0 V<sub>RHE</sub>, which is close to the measured value (6.18 mA cm<sup>-2</sup>, Fig. 2A). These demonstrations clearly reveal that the relatively high accuracy of the reported photocurrent density. Scanning photoelectrochemical microscopy (SPCEM) has been conducted to explore surface photocurrent changes on pristine Ta<sub>3</sub>N<sub>5</sub> and NiFe/Ta<sub>3</sub>N<sub>5</sub> photoanodes. As shown in Fig. S7A and B, a relatively low current was obtained when the probe approached to the surface of pristine Ta<sub>3</sub>N<sub>5</sub> regions. However, when the probe was moved to NiFe/Ta<sub>3</sub>N<sub>5</sub> regions, the photocurrent was remarkably increased, further indicating a stronger water oxidation ability of NiFe/Ta<sub>3</sub>N<sub>5</sub> than that of pristine Ta<sub>3</sub>N<sub>5</sub>.

The interfacial charge transfer and oxygen evolution kinetics were explored by electrochemical impedance spectroscopy (EIS) measurements. According to Nyquist plots and the fitting results (Fig. 2D, S8, and Table S2), NiFe/Ta<sub>3</sub>N<sub>5</sub> photoanodes exhibit a much lower resistance (292.3 Ω) than those of pristine Ta<sub>3</sub>N<sub>5</sub> (3556 Ω), Ni/Ta<sub>3</sub>N<sub>5</sub> (2557 Ω) and Fe/Ta<sub>3</sub>N<sub>5</sub> (2884 Ω), confirming that the synergistic effect of Ni and Fe catalysts could significantly promote interfacial charge transfer. Moreover, the charge injection efficiencies were evaluated by using H<sub>2</sub>O<sub>2</sub> as a hole scavenger and shown in Fig. 2E. Among these samples, the pristine Ta<sub>3</sub>N<sub>5</sub> photoanode shows a relatively low efficiency of 23% at 1.23 V<sub>RHE</sub>. After the decoration of Ni or Fe catalysts on Ta<sub>3</sub>N<sub>5</sub> photoanodes, the charge injection efficiencies could be increased up to 48% and 31%, respectively. Owing to the synergistic effect of Ni and Fe catalysts, NiFe/Ta<sub>3</sub>N<sub>5</sub> photoanodes exhibit a much higher charge injection efficiency of 86% at 1.23 V<sub>RHE</sub>. Furthermore, their electrochemical properties for water oxidation under dark conditions were studied and shown in Fig. 2F. Obviously, NiFe/Ta<sub>3</sub>N<sub>5</sub> gives a lower overpotential and higher water oxidation current than other Ta<sub>3</sub>N<sub>5</sub>-based photoanodes. It should be noted that compared with Fe/Ta<sub>3</sub>N<sub>5</sub> samples, Ni/Ta<sub>3</sub>N<sub>5</sub> exhibits the preferable electrochemical activity, revealing the superior water oxidation capability of Ni catalysts than that of Fe catalysts. Later, the PEC stabilities of all these Ta<sub>3</sub>N<sub>5</sub> photoanodes were measured at 1.23 V<sub>RHE</sub> under continuous illumination. As shown in Fig. S9, the photocurrent density of pristine Ta<sub>3</sub>N<sub>5</sub> photoanode significantly decreases upon initiating the light irradiation, and only 17% of initial activity could be obtained after 10 min illumination, suffering from the substitution of nitrogen atom with oxygen atom on Ta<sub>3</sub>N<sub>5</sub> photoanode surfaces. After the decoration of Ni and Fe catalysts, the PEC water oxidation stability of Ta<sub>3</sub>N<sub>5</sub> photoanode could be slightly enhanced. Amazingly, the photocurrent density of NiFe/Ta<sub>3</sub>N<sub>5</sub> photoanodes could be generally kept consistent during 30 min test, suggesting their relatively high structure stability. Thereby, the PEC activity and

durability of Ta<sub>3</sub>N<sub>5</sub> photoanodes could be significantly improved by the decoration of NiFe catalysts.

Kelvin probe force microscopy (KPFM) was employed to further explore the hole extraction ability of Ni and Fe catalysts from Ta<sub>3</sub>N<sub>5</sub> photoanodes. More specifically, the surface potential difference could effectively reflect the changes of the steady-state hole concentrations near the surfaces of Ta<sub>3</sub>N<sub>5</sub>-based photoanodes. To ensure the accuracy of the surface potential changes, the KPFM measurements were performed on same region under dark and illumination (The insets of height distribution). Fig. 3 and Fig. S10 show the typical topographic images and corresponding line scanning of surface potential changes under the darkness and illumination. It can be clearly observed that the pristine Ta<sub>3</sub>N<sub>5</sub> photoanodes exhibit a relatively low surface potential changes (72 mV), mainly suffered from the high charge recombination. After the decoration of Ni catalysts on Ta<sub>3</sub>N<sub>5</sub> photoanodes, the potential changes effectively were increased up to 143 mV. Amazingly, Fe/Ta<sub>3</sub>N<sub>5</sub> photoanodes shows a potential change of 206 mV, which is nearly similar to NiFe/Ta<sub>3</sub>N<sub>5</sub> samples (222 mV). This result clearly reveals that the Fe component in NiFe catalysts should play a crucial role in extracting hole from the bulk/surface of Ta<sub>3</sub>N<sub>5</sub> photoanodes for promote the charge separation and hole transfer.

The surface electron structures and chemical states of Ta<sub>3</sub>N<sub>5</sub> photoanodes after OER catalyst decoration were explored by X-ray photoelectron spectroscopy (XPS). As shown in Fig. 4A, Ta 4f and N 1s peaks of Ni/Ta<sub>3</sub>N<sub>5</sub>, Fe/Ta<sub>3</sub>N<sub>5</sub> and NiFe/Ta<sub>3</sub>N<sub>5</sub> photoanodes evidently shift toward high binding energy (BE) region compared with pristine Ta<sub>3</sub>N<sub>5</sub> photoanode. More specifically, the BE shifts of Ta 4f and N 1s peaks of Ni/Ta<sub>3</sub>N<sub>5</sub> photoanode are about 0.2 and 0.4 eV, respectively. Interestingly, the BE shifts of Ta 4f and N 1s peaks of Fe/Ta<sub>3</sub>N<sub>5</sub> photoanode could be achieved up to 0.5 and 0.6 eV, respectively, which are basically consistent with the BE shifts of NiFe/Ta<sub>3</sub>N<sub>5</sub> photoanodes. These demonstrations clearly reveal that compared with Ni catalysts, the Fe catalysts possess higher electron transfer ability from of Ta<sub>3</sub>N<sub>5</sub> photoanodes, which should be more efficient for promoting the charge separation and hole transfer. Thereby, it was considered that the decoration of NiFe-based catalysts could enrich the electron densities in Fe and Ni sites, which could effectively extract photogenerated holes from Ta<sub>3</sub>N<sub>5</sub> photoanodes under illumination. To further confirm the above speculation, the PEC performances of Ta<sub>3</sub>N<sub>5</sub> photoanodes with different deposition sequences of Ni and Fe catalysts have been explored. As shown in Fig. 4D, Ni/Fe/Ta<sub>3</sub>N<sub>5</sub> exhibits a photocurrent density of 10.2 mA cm<sup>-2</sup> at 1.23 V<sub>RHE</sub>, which is slightly lower than PEC activity of NiFe/Ta<sub>3</sub>N<sub>5</sub> samples (11.2 mA cm<sup>-2</sup>). Compared with Ni/Fe/Ta<sub>3</sub>N<sub>5</sub> samples (Fig. S13), NiFe/Ta<sub>3</sub>N<sub>5</sub> photoanodes possess more efficient charge separation, charge injection efficiency, and water oxidation ability, which might result in better catalytic performances of NiFe/Ta<sub>3</sub>N<sub>5</sub> than that of Ni/Fe/Ta<sub>3</sub>N<sub>5</sub>. Furthermore, note that the photocurrent density of Fe/Ni/Ta<sub>3</sub>N<sub>5</sub> photoanodes is much lower than that of NiFe/Ta<sub>3</sub>N<sub>5</sub> and Ni/Fe/Ta<sub>3</sub>N<sub>5</sub> samples, even lower than that of single Fe or Ni catalysts decorated Ta<sub>3</sub>N<sub>5</sub> photoanodes. These demonstrations clearly indicate that the deposition sequences of Ni and Fe catalysts play an important role in determining the PEC performances of Ta<sub>3</sub>N<sub>5</sub> photoanodes.

To further explore the contributions of Ni and Fe catalysts, more detailed PEC tests of Ni/Fe/Ta<sub>3</sub>N<sub>5</sub> and Fe/Ni/Ta<sub>3</sub>N<sub>5</sub> have been conducted. According to Nyquist plots and the fitting results (Figure S13D and Table S2), Ni/Fe/Ta<sub>3</sub>N<sub>5</sub> shows a much lower charge transfer resistance (R<sub>ct</sub>) of 546.4 Ω than Fe/Ni/Ta<sub>3</sub>N<sub>5</sub> (3035 Ω), which could effectively promote the charge separation efficiency. Meanwhile, Ni/Fe/Ta<sub>3</sub>N<sub>5</sub> exhibits a much higher charge injection efficiency than Fe/Ni/Ta<sub>3</sub>N<sub>5</sub> (Fig. S13E). Furthermore, their electrochemical OER properties under dark conditions have also been studied and shown in Figure S13F. Obviously, Ni/Fe/Ta<sub>3</sub>N<sub>5</sub> possesses a lower overpotential and higher water oxidation current compared with Fe/Ni/Ta<sub>3</sub>N<sub>5</sub>, further revealing the excellent OER activity of Ni/Fe catalysts. Combined with the experimental results of KPFM, it can be concluded that the preferred deposition of Fe catalysts nanolayers could promote the charge

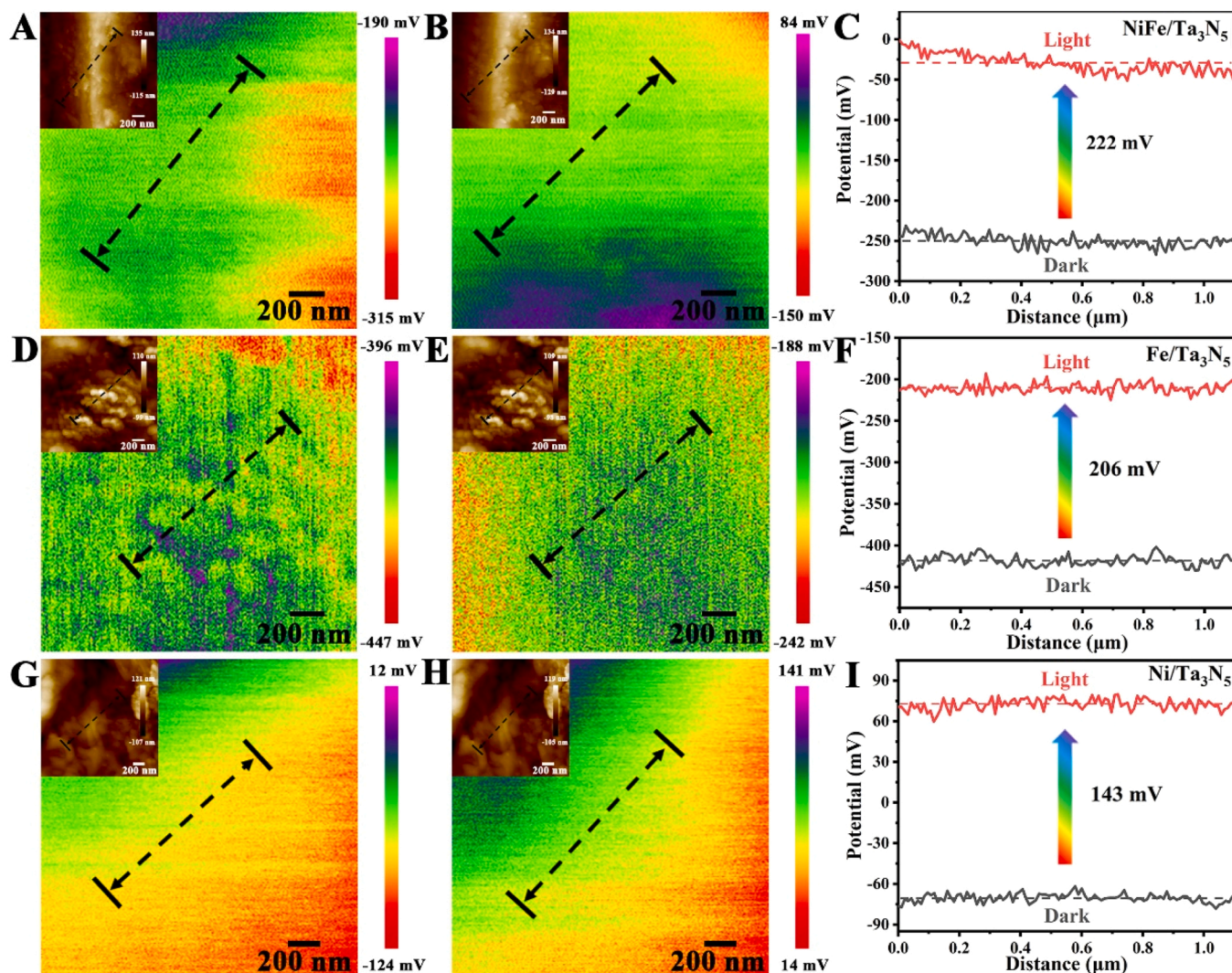


**Fig. 3.** KPFM of the surface potential distribution of NiFe/Ta<sub>3</sub>N<sub>5</sub>, Fe/Ta<sub>3</sub>N<sub>5</sub> and Ni/Ta<sub>3</sub>N<sub>5</sub> photoanodes (A, D, G) in dark and (B, E, H) under illumination, and (C, F, I) the comparison of the line-scanning surface potential in dark and illumination, respectively. The insets are height distribution of corresponding surface potential images.

separation and hole transfer, while the subsequent formation of Ni catalysts layers could provide the catalytic active-sites for water oxidation. Accordingly, their synergistic effects significantly improve the interfacial hole transfer and surface oxygen evolution kinetics, leading to an outstanding PEC water splitting activity. Additionally, the high-resolution energy dispersive spectroscopy has been employed to explore the elemental distributions of NiFe/Ta<sub>3</sub>N<sub>5</sub> photoanodes. As shown in Fig. S16, the line scanning energy spectrum clearly reveals that the distribution of Ni element is evidently larger than Fe element in the outer layer of NiFe/Ta<sub>3</sub>N<sub>5</sub> photoanodes, further confirming the preferred deposition of Fe catalysts than Ni catalysts.

On the basis of above results, it was speculated that the selective deposition of Fe catalysts and Ni catalysts on the Ta<sub>3</sub>N<sub>5</sub> photoanode surfaces should play a crucial role in determining the PEC water oxidation activity. Accordingly, we propose a possible mechanism to illustrate the photogenerated charge transfer and water oxidation reaction for the Ta<sub>3</sub>N<sub>5</sub>-based photoanodes in Scheme 1. Pristine Ta<sub>3</sub>N<sub>5</sub> shows the lowest photocurrent density due to its high charge recombination and poor surface reactivity. For Ni/Ta<sub>3</sub>N<sub>5</sub> and Fe/Ta<sub>3</sub>N<sub>5</sub>, they have only active-sites layer or hole transfer layer, respectively, resulting in their poor performance. Interestingly, because of the inappropriate order of Ni and Fe catalysts, neither of their respective roles can be performed effectively for Fe/Ni/Ta<sub>3</sub>N<sub>5</sub>. Conversely, both Ni/Fe/Ta<sub>3</sub>N<sub>5</sub>

and NiFe/Ta<sub>3</sub>N<sub>5</sub> exhibit outstanding PEC performance due to the rational order. More specifically, in the deposition process, Fe ions are preferentially deposited on Ta<sub>3</sub>N<sub>5</sub> accompanied by a small amount of Ni ions, and then Ni ions are subsequently deposited accompanied by a small amount of Fe ions. Under light excitation, due to the enrichment of electrons on Ni and Fe sites, the photogenerated holes migrate from Ta<sub>3</sub>N<sub>5</sub> to NiFe catalysts, while the photogenerated electrons would transfer through Ta substrate to the counter electrode. Then, holes migrate to the interface of NiFe catalysts and electrolyte. Water oxidation reaction occurs on the active sites of Ni and Fe. The synergistic effect of Ni catalysts and Fe catalysts could further enhance hole extraction ability and water oxidation ability of NiFe catalysts.

#### 4. Conclusion

In summary, a facile impregnation method has been developed to rationally decorate NiFe catalysts nanolayers on Ta<sub>3</sub>N<sub>5</sub> nanotube photoanodes, which exhibited an outstanding PEC activity for water oxidation (11.2 mA cm<sup>-2</sup> at 1.23 V<sub>RHE</sub>). The detailed experiment analysis reveals that the selective depositions of Fe and Ni catalysts on Ta<sub>3</sub>N<sub>5</sub> photoanode surfaces play important roles in promoting the PEC performances. More specifically, the preferred deposition of Fe catalysts nanolayers on Ta<sub>3</sub>N<sub>5</sub> photoanodes could effectively facilitate the charge



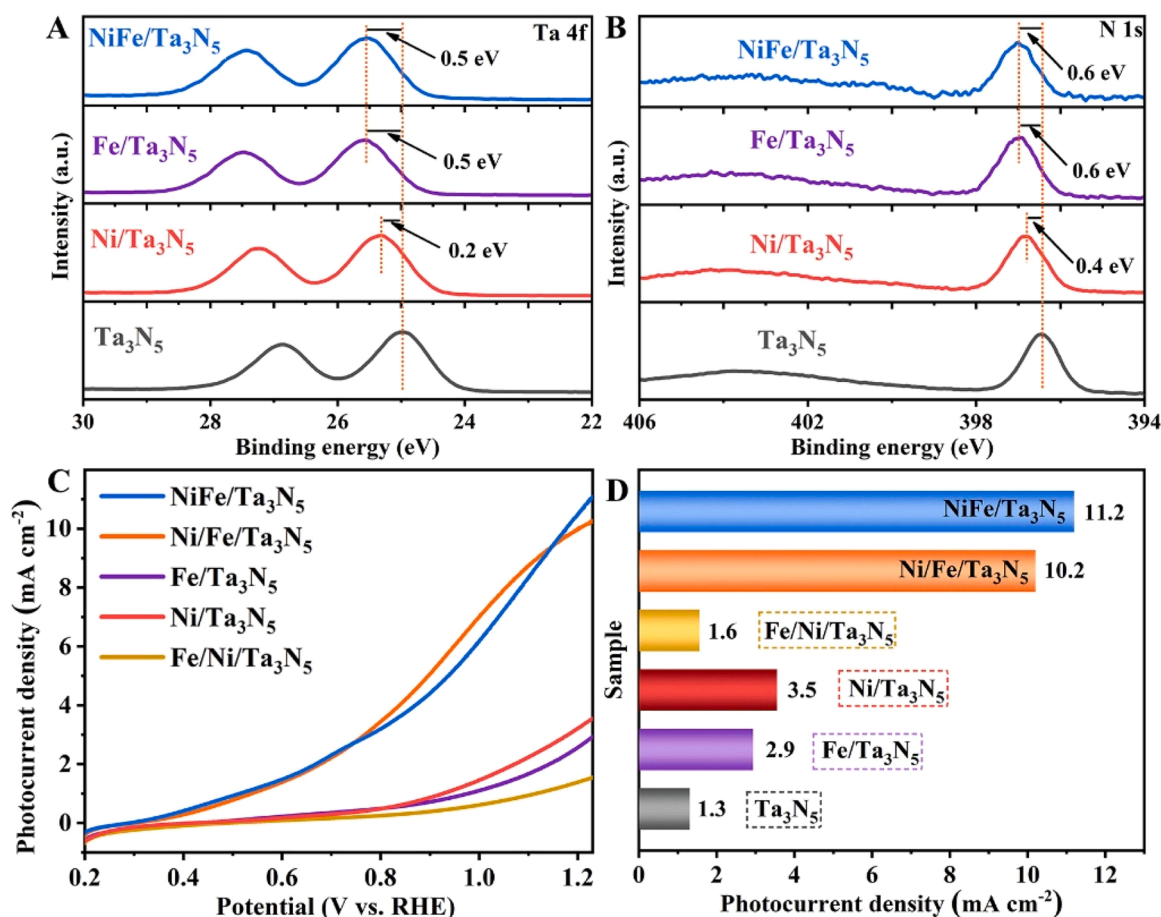
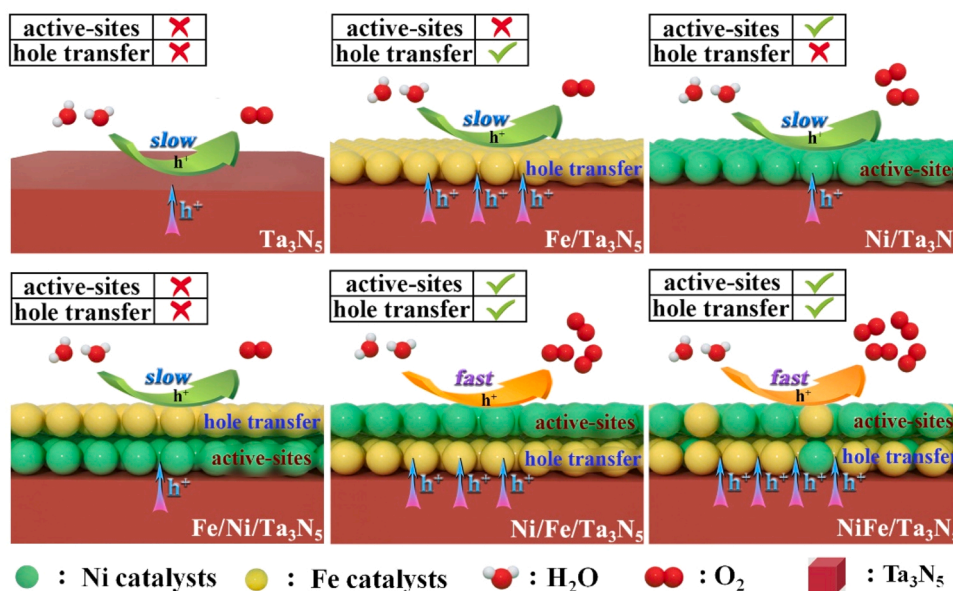


Fig. 4. XPS fine-structure spectra of (A) Ta 4f and (B) N 1s for various Ta<sub>3</sub>N<sub>5</sub>-based photoanodes. (C) LSV of deposition sequence control experiments and (D) photocurrent densities of all-prepared Ta<sub>3</sub>N<sub>5</sub>-based photoanodes measured at 1.23 V<sub>RHE</sub>.



Scheme 1. Schematic illustration of photogenerated charge transfer and water oxidation reaction for all-prepared Ta<sub>3</sub>N<sub>5</sub>-based photoanodes.

separation and hole transfer, while the subsequent formation of Ni catalysts layers could provide the catalytic active-sites for water oxidation. Benefiting from their synergistic effects, the interfacial hole transfer and surface oxygen evolution kinetics have been both

significantly improved, leading to an outstanding PEC water splitting activity. This work not only reported an effective approach for significantly promoting the PEC activity of Ta<sub>3</sub>N<sub>5</sub> photoanodes for water oxidation, but also highlighted the crucial roles of bimetallic catalyst,



which may provide important inspirations for fabricating highly efficient PEC water splitting devices.

### CRedit authorship contribution statement

**Congzhao Dong:** Investigation, Methodology, Formal analysis, Data curation, Writing – original draft. **Xian Zhang:** Investigation, Methodology, Formal analysis. **Yong Ding:** Writing – review & editing, Supervision, Funding acquisition. **Yajun Zhang:** Formal analysis, Data curation. **Yingpu Bi:** Investigation, Writing – review & editing, Project administration, Funding acquisition.

### Declaration of Competing Interest

The authors declare that they have no known competing financial interests or personal relationships that could have appeared to influence the work reported in this paper.

### Data Availability

Data will be made available on request.

### Acknowledgements

The work was supported by the National Natural Science Foundation of China (22075119, 21832005, 22072168, 22002175), the Natural Science Foundation of Gansu Province (21JR7RA440), Major Science and Technology Project of Gansu: (22ZD6GA003), and West Light Foundation of Chinese Academy of Sciences (xbzg-zdsys-202209). The authors also appreciate the assistance of Dr Shuqing Dong and Qing Liang for the SPECM and KPFM measurements.

### Appendix A. Supporting information

Supplementary data associated with this article can be found in the online version at [doi:10.1016/j.apcatb.2023.123055](https://doi.org/10.1016/j.apcatb.2023.123055).

### References

- [1] S. Wang, G. Liu, L. Wang, Crystal facet engineering of photoelectrodes for photoelectrochemical water splitting, *Chem. Rev.* 119 (2019) 5192–5247.
- [2] P. Zhou, I.A. Navi, Y. Ma, Y. Xiao, P. Wang, Z. Ye, B. Zhou, K. Sun, Z. Mi, Solar-to-hydrogen efficiency of more than 9% in photocatalytic water splitting, *Nature* 613 (2023) 66–70.
- [3] Y. Kuang, Q. Jia, G. Ma, T. Hisatomi, T. Minegishi, H. Nishiyama, M. Nakabayashi, N. Shibata, T. Yamada, A. Kudo, K. Domen, Ultrastable low-bias water splitting photoanodes via photocorrosion inhibition and in situ catalyst regeneration, *Nat. Energy* 2 (2016) 16191.
- [4] Y. Fu, C.-L. Dong, W. Zhou, Y.-R. Lu, Y.-C. Huang, Y. Liu, P. Guo, L. Zhao, W.-C. Chou, S. Shen, A ternary nanostructured  $\alpha\text{-Fe}_2\text{O}_3/\text{Au}/\text{TiO}_2$  photoanode with reconstructed interfaces for efficient photoelectrocatalytic water splitting, *Appl. Catal. B Environ.* 260 (2020), 118206.
- [5] Y. Fang, X. Li, Y. Wang, C. Giordano, X. Wang, Gradient sulfur doping along polymeric carbon nitride films as visible light photoanodes for the enhanced water oxidation, *Appl. Catal. B: Environ.* 268 (2020), 118398.
- [6] Y. Li, G. Xu, X. Zhu, Z. Man, X. Fu, Z. Hao, Y. Cui, C. Yuan, W. Zhang, S. Yan, H. Ge, Y. Chen, Z. Zou, A hierarchical dual-phase photoetching template route to assembling functional layers on Si photoanode with tunable nanostructures for efficient water splitting, *Appl. Catal. B: Environ.* 259 (2019), 118115.
- [7] T. Wang, Y. Wei, X. Chang, C. Li, A. Li, S. Liu, J. Zhang, J. Gong, Homogeneous  $\text{Cu}_2\text{O}$  p-n junction photocathodes for solar water splitting, *Appl. Catal. B Environ.* 226 (2018) 31–37.
- [8] S. Li, H. Lin, G. Yang, X. Ren, S. Luo, X.-s. Wang, Z. Chang, J. Ye, A synergetic strategy to construct anti-reflective and anti-corrosive  $\text{Co-P}/\text{WS}_2/\text{Si}$  photocathode for durable hydrogen evolution in alkaline condition, *Appl. Catal. B Environ.* 304 (2022), 120954.
- [9] D. Kang, T.W. Kim, S.R. Kubota, A.C. Cardiel, H.G. Cha, K.S. Choi, Electrochemical synthesis of photoelectrodes and catalysts for use in solar water splitting, *Chem. Rev.* 115 (2015) 12839–12887.
- [10] T.W. Kim, K.S. Choi, Nanoporous  $\text{BiVO}_4$  photoanodes with dual-layer oxygen evolution catalysts for solar water splitting, *Science* 343 (2014) 990–994.
- [11] C. Feng, S. Fu, W. Wang, Y. Zhang, Y. Bi, High-crystalline and high-aspect-ratio hematite nanotube photoanode for efficient solar water splitting, *Appl. Catal. B: Environ.* 257 (2019), 117900.
- [12] D.K. Lee, K.-S. Choi, Enhancing long-term photostability of  $\text{BiVO}_4$  photoanodes for solar water splitting by tuning electrolyte composition, *Nat. Energy* 3 (2017) 53–60.
- [13] S. Ye, W. Shi, Y. Liu, D. Li, H. Yin, H. Chi, Y. Luo, N. Ta, F. Fan, X. Wang, C. Li, Unassisted photoelectrochemical cell with multimediator modulation for solar water splitting exceeding 4% solar-to-hydrogen efficiency, *J. Am. Chem. Soc.* 143 (2021) 12499–12508.
- [14] C. Liu, J. Zhou, J. Su, L. Guo, Turning the unwanted surface bismuth enrichment to favourable  $\text{BiVO}_4/\text{BiOCl}$  heterojunction for enhanced photoelectrochemical performance, *Appl. Catal. B Environ.* 241 (2019) 506–513.
- [15] W.-J. Chun, A. Ishikawa, H. Fujisawa, T. Takata, J.N. Kondo, M. Hara, M. Kawai, Y. Matsumoto, K. Domen, Conduction and Valence Band Positions of  $\text{Ta}_2\text{O}_5$ ,  $\text{TaON}$ , and  $\text{Ta}_3\text{N}_5$  by UPS and electrochemical methods, *J. Phys. Chem. B* 107 (2003) 1798–1803.
- [16] Z. Wang, Y. Inoue, T. Hisatomi, R. Ishikawa, Q. Wang, T. Takata, S. Chen, N. Shibata, Y. Ikuhara, K. Domen, Overall water splitting by  $\text{Ta}_3\text{N}_5$  nanorod single crystals grown on the edges of  $\text{KTaO}_3$  particles, *Nat. Catal.* 1 (2018) 756–763.
- [17] M. Zhong, T. Hisatomi, Y. Sasaki, S. Suzuki, K. Teshima, M. Nakabayashi, N. Shibata, H. Nishiyama, M. Katayama, T. Yamada, K. Domen, Highly active GaN-stabilized  $\text{Ta}_3\text{N}_5$  thin-film photoanode for solar water oxidation, *Angew. Chem. Int. Ed.* 56 (2017) 4739–4743.
- [18] Y. He, James E. Thorne, Cheng H. Wu, P. Ma, C. Du, Q. Dong, J. Guo, D. Wang, What limits the performance of  $\text{Ta}_3\text{N}_5$  for solar water splitting? *Chem* 1 (2016) 640–655.
- [19] V. Nandal, Y. Pihosh, T. Higashi, T. Minegishi, T. Yamada, K. Seki, M. Sugiyama, K. Domen, Probing fundamental losses in nanostructured  $\text{Ta}_3\text{N}_5$  photoanodes: design principles for efficient water oxidation, *Energy Environ. Sci.* 14 (2021) 4038–4047.
- [20] Y. Kado, R. Hahn, C.-Y. Lee, P. Schmuki, Strongly enhanced photocurrent response for Na doped  $\text{Ta}_3\text{N}_5$ -nano porous structure, *Electrochem. Commun.* 17 (2012) 67–70.
- [21] J. Seo, T. Takata, M. Nakabayashi, T. Hisatomi, N. Shibata, T. Minegishi, K. Domen, Mg-Zr cosubstituted  $\text{Ta}_3\text{N}_5$  photoanode for lower-onset-potential solar-driven photoelectrochemical water splitting, *J. Am. Chem. Soc.* 137 (2015) 12780–12783.
- [22] S. Grigorescu, B. Bärhausen, L. Wang, A. Mazare, J.E. Yoo, R. Hahn, P. Schmuki, Tungsten doping of  $\text{Ta}_3\text{N}_5$ -nanotubes for band gap narrowing and enhanced photoelectrochemical water splitting efficiency, *Electrochem. Commun.* 51 (2015) 85–88.
- [23] J. Wang, Y. Jiang, A. Ma, J. Jiang, J. Chen, M. Li, J. Feng, Z. Li, Z. Zou, Charge compensation doping to improve the photocatalytic and photoelectrochemical activities of  $\text{Ta}_3\text{N}_5$ : a theoretical study, *Appl. Catal. B: Environ.* 244 (2019) 502–510.
- [24] Y. Kado, C.-Y. Lee, K. Lee, J. Muller, M. Moll, E. Spiecker, P. Schmuki, Enhanced water splitting activity of M-doped  $\text{Ta}_3\text{N}_5$  ( $M = \text{Na}, \text{K}, \text{Rb}, \text{Cs}$ ), *Chem. Commun.* 48 (2012) 8685–8687.
- [25] J. Fu, Z. Fan, M. Nakabayashi, H. Ju, N. Pastukhova, Y. Xiao, C. Feng, N. Shibata, K. Domen, Y. Li, Interface engineering of  $\text{Ta}_3\text{N}_5$  thin film photoanode for highly efficient photoelectrochemical water splitting, *Nat. Commun.* 13 (2022) 729.
- [26] Y. Hou, T. Li, S. Yan, Z. Zou, Oriented-growth  $\text{Ta}_3\text{N}_5/\text{SrTaO}_2\text{N}$  array heterojunction with extended depletion region for improved water oxidation, *Appl. Catal. B: Environ.* 269 (2020), 118777.
- [27] E. Nurlaela, Y. Sasaki, M. Nakabayashi, N. Shibata, T. Yamada, K. Domen, Towards zero bias photoelectrochemical water splitting: onset potential improvement on a Mg:Ga modified- $\text{Ta}_3\text{N}_5$  photoanode, *J. Mater. Chem. A* 6 (2018) 15265–15273.
- [28] S. Grigorescu, S. So, J.E. Yoo, A. Mazare, R. Hahn, P. Schmuki, Open top anodic  $\text{Ta}_3\text{N}_5$  nanotubes for higher solar water splitting efficiency, *Electrochim. Acta* 182 (2015) 803–808.
- [29] L. Jin, F. Cheng, H. Li, K. Xie, Porous tantalum nitride single crystal at two-centimeter scale with enhanced photoelectrochemical performance, *Angew. Chem. Int. Ed.* 59 (2020) 8891–8895.
- [30] Y. Zhao, H. Xie, W. Shi, H. Wang, C. Shao, C. Li, Unravelling the essential difference between  $\text{TiO}_x$  and  $\text{AlO}_x$  interface layers on  $\text{Ta}_3\text{N}_5$  photoanode for photoelectrochemical water oxidation, *J. Energy Chem.* 64 (2022) 33–37.
- [31] Y. Xiao, C. Feng, J. Fu, F. Wang, C. Li, V.F. Kunzelmann, C.-M. Jiang, M. Nakabayashi, N. Shibata, I.D. Sharp, K. Domen, Y. Li, Band structure engineering and defect control of  $\text{Ta}_3\text{N}_5$  for efficient photoelectrochemical water oxidation, *Nat. Catal.* 3 (2020) 932–940.
- [32] M.G. Walter, E.L. Warren, J.R. McKone, S.W. Boettcher, Q. Mi, E.A. Santori, N. S. Lewis, Solar water splitting cells, *Chem. Rev.* 110 (2010) 6446–6473.
- [33] K. Dang, X. Chang, T. Wang, J. Gong, Enhancement of photoelectrochemical oxidation by an amorphous nickel boride catalyst on porous  $\text{BiVO}_4$ , *Nanoscale* 9 (2017) 16133–16137.
- [34] J. Quinero, R. Gómez, Controlling the amount of co-catalyst as a critical factor in determining the efficiency of photoelectrodes: The case of nickel (II) hydroxide on vanadate photoanodes, *Appl. Catal. B: Environ.* 217 (2017) 437–447.
- [35] P. Wen, R. Lei, X. Cao, Q. Ma, G. Zhang, C. Guo, X. Wang, Y. Qiu, Anchored Ni nanocrystals boosting  $\text{BiVO}_4$  photoanode for highly efficient water oxidation via in-situ generation of  $\text{Ni}(\text{NiOOH})$  co-catalyst, *Chem. Eng. J.* 454 (2023), 139983.
- [36] B. Zhang, L. Wang, Y. Zhang, Y. Ding, Y. Bi, Ultrathin  $\text{FeOOH}$  nanolayers with abundant oxygen vacancies on  $\text{BiVO}_4$  photoanodes for efficient water oxidation, *Angew. Chem. Int. Ed.* 57 (2018) 2248–2252.
- [37] F. Yu, F. Li, T. Yao, J. Du, Y. Liang, Y. Wang, H. Han, L. Sun, Fabrication and kinetic study of a ferrihydrite-modified  $\text{BiVO}_4$  photoanode, *ACS Catal.* 7 (2017) 1868–1874.

- [38] T.-G. Vo, Y. Tai, C.-Y. Chiang, Novel hierarchical ferric phosphate/bismuth vanadate nanocactus for highly efficient and stable solar water splitting, *Appl. Catal. B: Environ.* 243 (2019) 657–666.
- [39] R. Chen, C. Zhen, Y. Yang, X. Sun, J.T.S. Irvine, L. Wang, G. Liu, H.-M. Cheng, Boosting photoelectrochemical water splitting performance of  $\text{Ta}_3\text{N}_5$  nanorod array photoanodes by forming a dual co-catalyst shell, *Nano Energy* 59 (2019) 683–688.
- [40] Y. Li, T. Takata, D. Cha, K. Takanabe, T. Minegishi, J. Kubota, K. Domen, Vertically aligned  $\text{Ta}_3\text{N}_5$  nanorod arrays for solar-driven photoelectrochemical water splitting, *Adv. Mater.* 25 (2013) 125–131.
- [41] X. Cao, C. Xu, X. Liang, J. Ma, M. Yue, Y. Ding, Rationally designed/assembled hybrid  $\text{BiVO}_4$ -based photoanode for enhanced photoelectrochemical performance, *Appl. Catal. B Environ.* 260 (2020), 118136.
- [42] B. Zhang, L. Chou, Y. Bi, Tuning surface electronegativity of  $\text{BiVO}_4$  photoanodes toward high-performance water splitting, *Appl. Catal. B Environ.* 262 (2020), 118267.
- [43] Q. Sun, T. Cheng, Z. Liu, L. Qi, A cobalt silicate modified  $\text{BiVO}_4$  photoanode for efficient solar water oxidation, *Appl. Catal. B Environ.* 277 (2020), 119189.
- [44] Y. Pihosh, T. Minegishi, V. Nandal, T. Higashi, M. Katayama, T. Yamada, Y. Sasaki, K. Seki, Y. Suzuki, M. Nakabayashi, M. Sugiyama, K. Domen,  $\text{Ta}_3\text{N}_5$ -Nanorods enabling highly efficient water oxidation via advantageous light harvesting and charge collection, *Energy Environ. Sci.* 13 (2020) 1519–1530.
- [45] Z. Shi, J. Feng, H. Shan, X. Wang, Z. Xu, H. Huang, Q. Qian, S. Yan, Z. Zou, Low onset potential on single crystal  $\text{Ta}_3\text{N}_5$  polyhedron array photoanode with preferential exposure of {001} facets, *Appl. Catal. B: Environ.* 237 (2018) 665–672.
- [46] G. Liu, S. Ye, P. Yan, F. Xiong, P. Fu, Z. Wang, Z. Chen, J. Shi, C. Li, Enabling an integrated tantalum nitride photoanode to approach the theoretical photocurrent limit for solar water splitting, *Energy Environ. Sci.* 9 (2016) 1327–1334.
- [47] X. Zhang, H. Guo, G. Dong, Y. Zhang, G. Lu, Y. Bi, Homostructural  $\text{Ta}_3\text{N}_5$  nanotube/nanoparticle photoanodes for highly efficient solar-driven water splitting, *Appl. Catal. B: Environ.* 277 (2020), 119217.
- [48] M. Li, W. Luo, D. Cao, X. Zhao, Z. Li, T. Yu, Z. Zou, A co-catalyst-loaded  $\text{Ta}_3\text{N}_5$  photoanode with a high solar photocurrent for water splitting upon facile removal of the surface layer, *Angew. Chem. Int. Ed.* 52 (2013) 11016–11020.
- [49] L. Wang, B. Zhang, Q. Rui, Plasma-Induced vacancy defects in oxygen evolution cocatalysts on  $\text{Ta}_3\text{N}_5$  photoanodes promoting solar water splitting, *ACS Catal.* 8 (2018) 10564–10572.
- [50] B. Zhang, X. Huang, Y. Zhang, G. Lu, L. Chou, Y. Bi, Unveiling the activity and stability origin of  $\text{BiVO}_4$  photoanodes with FeNi oxyhydroxides for oxygen evolution, *Angew. Chem. Int. Ed.* 59 (2020) 18990–18995.